Hinode, TRACE, SOHO and ground-based observations of a quiescent prominence

P. Heinzel

Astronomical Institute, Academy of Sciences of the Czech Republic, 25165 Ondřejov, Czech Republic

`pheinzel@asu.cas.cz`

B. Schmieder

Observatoire de Paris, Section Meudon, LESIA, 92195 Meudon Principal Cedex, France

F. Fárník, P. Schwartz

Astronomical Institute, Academy of Sciences of the Czech Republic, 25165 Ondřejov, Czech Republic

N. Labrosse

Department of Physics and Astronomy, University of Glasgow, G128QQ Scotland, United Kingdom

P. Kotrč

Astronomical Institute, Academy of Sciences of the Czech Republic, 25165 Ondřejov, Czech Republic

U. Anzer

Max-Planck-Institut für Astrophysik, Karl-Schwarzschild-Strasse 1, 85740 Garching, Germany

G. Molodij

Observatoire de Paris, Section Meudon, LESIA, 92195 Meudon Principal Cedex, France

A. Berlicki

Astronomical Institute of the Wrocław University, Kopernika 11, 51-622 Wrocław, Poland

E. E. DeLuca, L. Golub

Center for Astrophysics, 60 Garden Street, Cambridge, MA 02138, USA

T. Watanabe

National Astronomical Observatory of Japan, Mitaka, Tokyo, 181-8588, Japan

T. Berger

Lockheed Martin Solar and Astrophysics Laboratory, B/252, 3251 Hanover Street, Palo Alto, CA 94304, USA

ABSTRACT

A quiescent prominence was observed by several instruments on 2007 April 25. The temporal evolution was recorded in Hα by Hinode/SOT, in X-rays by Hinode/XRT and in the 195 Å channel by TRACE. Moreover, ground-based observatories (GBO) provided calibrated Hα intensities. Simultaneous EUV data were also taken by the Hinode/EIS and SOHO/SUMER-CDS spectrometers. Here we have selected the SOT Hα image taken at 13:19 UT which nicely shows the prominence fine structure. We compare this image with co-temporal ones taken by XRT and TRACE and show the intensity variations along several cuts parallel to the solar limb. EIS spectra were obtained about half an hour later. Dark prominence structure clearly seen in the TRACE and EIS 195 Å images is due to the prominence absorption in HI, HeI and HeII resonance continua plus the coronal emissivity blocking due to the prominence void (cavity). The void clearly visible in XRT images is entirely due to X-ray emissivity blocking, since no prominence structure is seen in the XRT images because of negligible absorption at X-ray wavelengths. We use TRACE, EIS and XRT data to estimate the amount of absorption and blocking. Independently, the Hα integrated intensities provide us with an estimate of the Hα opacity and this is related to the opacity of resonance continua as follows from the non-LTE radiative-transfer modeling. Therefore, we have an independent check of the results obtained from TRACE/XRT and EIS/XRT. However, spatial averaging of the Hα and EUV data have quite different natures which must be taken into account when evaluating the true opacities. We demonstrate this important effect here for the first time. Finally, based on this multi-wavelength analysis, we discuss the determination of the column densities and the ionization degree of hydrogen in the prominence.

Subject headings: prominences – XUV images – absorption/blocking – Hα emission

1. Introduction

Spectral observations of solar prominences reveal different aspects of their physical structure according to the lines and continua that are detected (Heinzel 2007a). The majority of prominence emission lines is formed in cooler parts by scattering of the incident radiation coming from the photosphere, chromosphere and transition region depending on the line-formation conditions. When observed above the limb, prominences typically appear as bright features against the dark corona. This is the case for chromospheric lines like Hα and other Balmer lines, Ca lines and others, but also for many transition-region lines formed inside the prominence-corona transition region (PCTR). Analysis of such optical and UV/EUV emission lines and continua, based on detailed non-LTE radiative-transfer modeling, can provide us with diagnostics of prominence thermodynamic parameters and the ionization state of the prominence plasma (Heinzel 2007b).

However, some important prominence parameters can also be deduced in a relatively simpler and more straightforward way which consists in analysis of the coronal-brightness reduction typically observed at prominence positions. It was shown by Daw et al. (1995) (see also the references therein) that the cool chromospheric material seen above the limb can absorb the XUV coronal radiation. For limb prominences this absorption was studied by Daw et al. (1995), and by Kucera et al. (1998) who used the SOHO/CDS observations of selected coronal lines. This method was then further developed and one can currently distinguish in the literature two complementary approaches which we may denote the 'patrol-type' approach and the 'multi-wavelength' approach. The first approach, 'patrol-type' studies, uses the simplest possible observations, typically only in one coronal line obtained by patrol--like instruments. The advantage is that instruments such as the SOHO/EIT or TRACE provide large field-of-view images and can be used to study many different objects and events, including the eruptive prominences which may be related to CMEs. A great disadvantage of the method is a significant limitation in diagnostics capabilities. For this kind of technique see e.g. Golub et al. (1999), Mein et al. (2001), Engvold et al. (2001) or the recent work of Gilbert et al. (2005, 2006) and Kucera & Landi (2008). On the other hand, the 'multi-wavelength approach tries to use as many coronal lines as possible, detected by various space instruments in the UV and EUV (SOHO, TRACE, Hinode/EIS), together with the broadband X-rays observed by Yohkoh/SXT and now by Hinode/XRT, to disentangle the absorption from the emissivity blocking mechanisms and to derive the hydrogen and helium ionization structure of prominences. The great advantage of such an approach is that it reduces the number of unknown quantities which appear in the respective equations. However, these observations require a substantional coordinated effort and planning, and they are usually made in the context of special campaigns, so that only a very few such data sets are available. Moreover, EUV spectrometers such as SUMER, CDS or EIS provide slit spectra and rasters are required

for sufficient spatial coverage, taking a rather long time to complete. Using SOHO and Yohkoh instruments, this type of study was performed by Kucera et al. (1998), Schmieder et al. (1999) or recently Anzer et al. (2007). There are several other similar studies devoted to filaments on the disk, see e.g. Heinzel et al. (2001), Schmieder et al. (2003) or Schwartz et al. (2004).

Two basic mechanisms lead to a coronal brightness reduction at the position of a prominence: absorption and emissivity blocking. The absorption of the coronal line radiation in EUV is due to the photoionization of hydrogen H (hydrogen Lyman continuum below 912 Å), neutral helium He I (resonance continuum below 504 Å) and ionized helium He II (resonance continuum below 228 Å). Theoretical aspects of this mechanism were summarized by Anzer & Heinzel (2005) who also give the model relations to the Hα line opacity. Observing suitably selected lines below 912 Å one can in principle diagnose the column densities of H, He I and He II. The densities derived in this way can be subsequently used to constrain sophisticated non-LTE models of hydrogen and helium line and continuum formation (Labrosse & Gouttebroze 2004, Heinzel et al. 2005, Gunár et al. 2007). The second mechanism responsible for lowering the brightness of EUV coronal lines is the 'emissivity blocking' first discussed in detail by Heinzel et al. (2003) and extensively applied to a filament study by Schwartz et al. (2004). This blocking is due to the fact that cool structures (prominences) or low-density structures (cavities, voids) in the corona exhibit much reduced emissivity or lack of it in the EUV lines. Anzer & Heinzel (2005) developed a theoretical formulation of the emissivity blocking due to the presence of cool prominence plasmas. Some aspects of the absorption and blocking were recently considered by Gilbert et al. (2005). In subsequent work Anzer et al. (2007) realized that the limb prominences are transparent in soft X-rays and suggested using this for a determination of the amount of emissivity blocking. Their study was based on Yohkoh/SXT observations of a coronal cavity in which the prominence was located (and observed by SOHO/EIT and SUMER)

Based on our previous work and experience, we have suggested using the capabilities of the Hinode mission for study of prominence absorption and emissivity blocking mechanisms, which in turn can provide useful diagnostics of the ionization state and column densities of hydrogen and helium. Multi-wavelength diagnostics are based on Hinode/EIS (EUV imaging spectrometer) and XRT (X-ray telescope) observations which are complemented by data from the TRACE, SOHO and Hinode/SOT (Solar optical telescope) instruments and ground-based Hα observations. To collect such multi-wavelength data, we organized coordinated observations among all of these instruments, as part of the HOP0004 and JOP 178 (study of filaments and prominences) programs.

In Section 2 the observations from space as well as from the ground, obtained during

the 2007 April coordinated campaign of Hinode and SOHO/SUMER (running JOP 178) are presented. In Section 3, the two mechanisms responsible for lowering the coronal EUV line intensities and soft X-ray brightness (absorption and emissivity blocking) are described, and we show the observed intensity contrasts of 195 Å coronal lines and X-rays. Opacities deduced from EUV contrasts are discussed in Section 4 while those corresponding to the Hα line are the subject of Section 5. In Section 6 we derive the optical thickness of the hydrogen Lyman continuum. In Section 7 we discuss our results and make estimates of the hydrogen column densities. In Conclusions (Section 8) we summarize our results and propose new multi-wavelength observations which would represent a next step in satisfying the complex diagnostic requirements. In this paper we also show for the first time how the spatial averaging of the prominence intensity can affect the determination of opacities, namely in the case of the coronal-line absorption model (Appendix).

2. Observations

The observations presented in this paper were obtained during a coordinated campaign of prominence studies involving SOT, XRT and EIS on Hinode, MDI, EIT, SUMER and CDS on SOHO, TRACE, and several ground-based observatories. These observations were obtained as part of HOP004 and JOP 178, between 2007 April 23 – 29. This was the first Hinode-SUMER observing campaign. HOP004 and JOP 178 are dedicated to the study of prominences and filaments, investigating various aspects of their three-dimensional structure and their magnetic environment from the photosphere to the corona (see http://gaia.bagn.obs-mip.fr/jop178/index.html).

2.1. Hinode SOT, XRT and EIS, TRACE

The Hinode mission is operating since October 2006 (Kosugi et al. 2007). The prominence under study was well observed on 2007 April 25 by the Hinode/SOT (Solar Optical Telescope) instrument, between 13:04 and 13:59 UT in the Hα and Ca II H lines. The 50 cm aperture telescope can obtain a continuous, seeing-free series of diffraction-limited images in the 3880 – 6680 Å range with 0.16-0.28 arcsec spatial resolution (see Suematsu et al. 2008). In our study we use only the Hα images (160 × 160 arcsec) recorded as a 1024 × 1024 pixel matrix, each pixel having dimensions of 0.16 × 0.16 arcsec. Center of the field of view in solar coordinates was [830, −510] arcsec and the exposure time was 0.3 s. The images are the Level-1 calibrated Hα filtergrams. They have been dark subtracted, flat-fielded and corrected for camera read-out anomalies. The flat-fielding procedure removes the fringes

due to reflections in the CCD chip. The image obtained at time 13:19 UT is shown in the left panel in Fig. 1. The field of view of the Ca II H image is smaller (108×108 arcsec) and does not cover the entire prominence. Fine structures of the prominence evolve rapidly, especially the round-shaped features at the bottom (Berger et al. 2008). They are rising and with their quasi-spherical shapes they resemble magnetic separatrices. The material in the prominence lying above these features is very dynamic as they move up. The fine-structure blobs typically move downward. This highly structured and dynamic behaviour can be seen in the respective SOT movie and we plan to discuss it in another paper.

The Hinode/XRT (X-ray Telescope) is a high-resolution grazing-incidence telescope which consists of the X-ray and visible light optics and uses the $2k \times 2k$ CCD camera. A set of filters and a broad range of exposure times enables the telescope to see hot plasmas in the range from 10^5 to 10^8 K. For more details see Golub et al. (2007). Observations of the prominence on 2007 April 25 were done between 13:02 and 13:59 UT with the 512×512 pixels coverage, each pixel having size of 1.03×1.03 arcsec. Filter combination was Al_{poly}/Open. The exposure time was 8.19 or 16.38 s, the cadence 60 s.

The Hinode/EIS (EUV Imaging Spectrometer) is described in detail in Culhane et al. (2007). It observes in two wavelength bands ($170 - 211$ Å and $246 - 292$ Å). Each band has a distinct 1024×2048 pixel CCD detector. The study used in this work is `fil_rast_s2`, which makes a large raster of 240×256 arcsec centered on the prominence with the 2 arcsec slit. At each slit position, a spectrum is obtained with a 50 s exposure. Data from 11 spectral windows is sent back from the satellite: 10 narrow spectral windows (32 pixels wide or 0.714 Å), along with a full spectrum on CCD B of EIS in the wavelength region between 189 Å and 211 Å. The raster used for this work started at 13:02 UT and the prominence region was scanned between 13:34 UT and 13:54 UT. All the relevant data from EIS has been corrected using the software provided by SolarSoft. This includes dark current subtraction, cosmic ray removal, flat field correction, flagging hot pixels, as well as absolute intensity calibration. We also coaligned the observations obtained through the two detectors. Because of the way the instrument is designed, raster images obtained in the short wavelengths are offset to solar north-west of the long wavelength images. The He II 256.32 Å line is used for co-alignment between SOT and EIS, and the heliocentric coordinates stored in the headers of the FITS files thus refer to this line. For these observations, we measure an offset of 1 pixel (2 arcsec) in the X direction and 19 pixels (19 arcsec) in the Y direction. EIS rasters show a vertical black stripe which unfortunately crosses the prominence. These dark pixels are spectra taken during the night period of the EIS instrument. EIS is an EUV instrument and the telluric atmosphere at a height of 50 km above sea level absorbs the EUV light from the Sun. In order to remove these dark pixels, we first correct the data at the extreme southern part of the raster image where the corona does not show any feature. We then apply the same

correction at all heights. The resulting image is satisfying and the prominence structure is clearly similar to what is seen on the TRACE picture. In addition to the vertical dark stripe there is also a horizontal stripe with an intensity depression (see panel b) in Fig. 3). This depression is seen only in the intensity integrated over the whole TRACE 195 Å bandpass (see Fig. 2), and it is not seen in the Fe XII 195 Å line alone (compare dashed-line and dotted-line plots in Fig. 7). Due to this fact we assume that this horizontal stripe is caused by some anomaly on the detector. We did not correct data for this stripe because it passes outside the prominence (we instead did not use the data from this part of the raster).

The NASA Transition Region And Coronal Explorer (TRACE) is a 30 cm aperture Cassegrain normal incidence telescope with 8.5×8.5 arcmin field of view and 1 arcsec spatial resolution. Its CCD detector has 1024×1024 pixels of angular size 0.5 arcsec. For further instrumental details see Handy et al. (1999). Our prominence was observed in the 195 Å bandpass, which enables us to see the plasma with temperature between 0.5 and 2 MK. The prominence was observed between 13:02 and 13:59 UT, the center of the field of view was at the solar coordinates $[799, -609]$ arcsec and the size of the images during that period is 768×768 pixels (384×384 arcsec).

2.2.   Coalignment of different observations

In our analysis we used the SOT Level-1 data in which no correction on instrument misalignment was applied. We defined the SOT/Hα image at 13:19 UT as the reference image because all of the instruments were pointing at the prominence at this time (apart from EIS which was rastering another part of the field of view and detected the prominence region only later). The movies from SOT show an extreme fine-structure activity in the prominence and thus the overlay should be done for very similar times in order to achieve good accuracy in the measurements. The prominence seen in Hα at this time had a few very well pronounced features and one of them – a nearly round-shaped dark opening (hole) – was also clearly visible in the TRACE 195 Å images as a bright hole within the dark prominence. Therefore, we could use this feature to make an overlay of the TRACE image over the Hα one (both taken at the same time) by adjusting the TRACE image so that the 'openings' precisely overlaid. This enabled us to correct the coordinates of the center of the field of view of the TRACE image. Next, we made a new overlay – the XRT image over the TRACE one (using its corrected coordinates) so that a few bright disk or near-limb features (dots) visible in both images coincided. Again, we could correct the coordinates of the center of field-of-view of the XRT image and could overlay SOT/Hα and XRT (Fig. 1). Finally, we had all four data sets (SOT/Hα , XRT, EIS and TRACE) in the same coordinate

system. This enabled us to make precise comparison between any of the images and, also, to make cuts through the prominence (i.e. to obtain the intensity profiles) along the same lines in all of the data sets (Fig. 3). In order to compare TRACE and EIS observations at 195 Å we multiplied the EIS spectrum between 189 Å and 201 Å (shown in Fig. 2) with the TRACE spectral response function (see Fig. 11 in Handy et al. 1998). Note that no continuum emission is detected in the EIS spectrum at these wavelengths (see also Labrosse et al. 2008).

2.3. SOHO CDS and SUMER

The SOHO/CDS (Harrison et al. 1995) spectrograph observed the prominence between 13:02:45 – 13:31:02 UT. The dimension of the rasters is 244×240 arcsec. The size of the raster pixel was 4×3.3 arcsec. Observations were made in 7 spectral lines (ordered from the lower to higher formation temperature, the wavelengths in parentheses are given according to CHIANTI database (Dere et al. 1997; Landi & Phillips 2006): He I 584.33 Å (584.335 Å), O IV 554.40 Å (554.513 Å plus other three, ten times fainter, O IV lines), O V 629.15 Å (629.732 Å), Ca X 558.48 Å (557.766 Å), Mg X 625.04 Å (624.943 Å), Si XII 521.27 Å (520.666 Å) and Fe XIX 592.77 Å (592.236 Å). The data were reduced and calibrated in erg cm^{-2} sec^{-1} sr^{-1} Å^{-1} using standard SolarSoft procedures for CDS calibration. Along the cuts across the prominence the integrated intensities for each observed line were computed.

The prominence was also observed by the SOHO/SUMER (Wilhelm et al. 1995) spectrograph in the hydrogen Lyman line series from Lyβ to Lyman continuum. On 2007 April 25, SUMER observed the prominence only after 17:48 UT. This is too far in time from other instrument observations and, therefore, we did not use these data here. However, in a future work we plan to use them for analysis of prominence fine structures (as in Gunár et al. 2007).

2.4. Ground-based observations

Two instruments were used for simultaneous ground-based observations: the imaging Multi-channel Subtractive Double Pass (MSDP) spectrograph in Meudon took 2D maps of the Hα line profiles, and the Zeiss' high-dispersion spectrograph with horizontal telescope – HSFA (Horizontal Sonnen-Forschungs Anlage) at Ondřejov Observatory recorded spectra in several lines, including Hα.

With the MSDP spectrograph operating on the Solar Tower of Meudon Observatory, the prominence was observed for three consecutive days, on 2007 April 24, 25 and 26. On

April 25 the prominence was observed between 12:09 and 13:32 UT. The entrance slit of the spectrograph covers an elementary field of view of 72×465 arcsec with a pixel size of 0.4 arcsec. The final field of view of the images is 500×465 arcsec. The exposure time was 250 ms. We performed consecutive sequences of 60 images with a cadence of 30 s. The spatial resolution is estimated to be between 1 and 2 arcsec, depending on the actual seeing conditions. Using the MSDP technique (Mein 1977, 1991) the Hα image of the field of view is split in wavelength into nine images covering the same field of view. The nine images are recorded simultaneously on a CCD camera. Each image is obtained in a different wavelength interval and the wavelength separation between images is 0.3 Å. By interpolating with spline functions between the observed intensities in these images, we are able to construct the Hα profile at each point of the observed field of view. A mean or reference disk profile is obtained by averaging over a quiet region on the disk in the vicinity of the prominence (in this case at $\sin\theta$=0.9). The photometric calibration is done by fitting the reference profile to standard profiles for the quiet Sun (David 1961). We corrected the image for scattered light by analysing the emission of the nearby corona. The prominence observations in Hα line center by the MSDP spectrograph are well coaligned with the SOT Hα images obtained at the same time (Fig. 4).

The prominence was also observed with the new multi-channel HSFA spectrograph of the Ondřejov Observatory, between 11:17 and 14:00 UT. Four lines Hα, Hβ, D3, Ca II K or Ca II H, together with the Hα slit-jaw image, were detected as the prominence was scanned. The diffraction grating enables a spectral resolution of 25 mÅ. The data acquisition system consists of five fast CCD cameras having the 1280×1024 pixel matrix. Exposure time of 150 ms was used for individual spectra. HSFA diffraction-limit resolution is better than 1 arcsec, however in these observations it was degraded due to seeing to some 3 arcsec. A standard width of the spectrograph slit for Hα is 100 μm and the scale of 0.17 mm at the solar image on the slit corresponds to 1 arcsec. For a description of the HSFA instrument see Kotrč (2007).

3. Absorption and emissivity blocking

3.1. Mechanisms of lowering the coronal brightness

Solar prominences observed above the solar limb are usually bright objects seen against a dark coronal background (Fig. 5). This is the case when the spectral observations (rasters or filtergrams) are made in optical lines like Hα or in transition-region lines. Optical lines are formed in central cool parts of the structure where hydrogen and helium are only partially ionized. Transition-region lines are formed in the prominence-corona transition region

(PCTR) at much higher temperatures. Quite a different situation takes place when prominences are observed in coronal lines, i.e. lines of highly ionized metals such as Mg X, Ca X, Si XII, Fe XII etc. The prominence itself does not emit radiation in these lines, but the coronal radiation behind the prominence can be strongly absorbed by the hydrogen and helium resonance continua due to the photoionization process. One has to consider the hydrogen Lyman continuum (head at $912\,\text{Å}$), He I continuum (head at $504\,\text{Å}$) and He II continuum (at $228\,\text{Å}$). The above mentioned lines detected by CDS are affected only by the hydrogen Lyman continuum, while the TRACE $195\,\text{Å}$ channel (FeXI and FeXII lines) is affected by all three continua. Ideally, using these observations, one could disentangle between hydrogen and helium opacities. A detailed quantitative description of this *absorption mechanism* which leads to a reduction in the coronal brightness at the location of the prominence is presented in Anzer & Heinzel (2005) (see other references therein).

Using the optical thickness τ_{912} at the hydrogen Lyman continuum head as a reference, we can write for τ at the wavelength position of any EUV coronal lines

$$\frac{\tau}{\tau_{912}} = \frac{\sigma_{\text{H}}}{\sigma_{\text{H}}(912)} + \frac{r_{\text{He}}}{1-i}\left[(1 - j_1 - j_2)\frac{\sigma_{\text{HeI}}}{\sigma_{\text{H}}(912)} + j_1\frac{\sigma_{\text{HeII}}}{\sigma_{\text{H}}(912)}\right],\tag{1}$$

where σ is the photoionization cross-section (see Anzer & Heinzel 2005), r_{He} is the helium abundance which we set to 0.1, i is the hydrogen ionization degree and j_1 and j_2 are the neutral and singly ionized helium ionization degrees, respectively. This formula allows us to determine the optical-thickness or opacity ratios for any set of these parameters. τ_{912} can be determined from CDS observations or using the theoretical correlation with $\tau_{\text{o}}(\text{H}\alpha)$.

The other mechanism which may lower the coronal brightness in EUV lines is the *emissivity blocking*. The coronal emissivity in EUV lines is depressed (or blocked) by the presence of the cool prominence material or low-density cavity (void) around the prominence. This mechanism together with the absorption lowers the coronal brightness – see the cartoon in Fig. 5. If the contrast r is the ratio of the intensity at the prominence position I_p to that outside (in the corona I_c or even within the cavity I'_c) and r_{b} is the ratio between coronal emission at the same position but at a wavelength where negligible absorption takes place (only blocking), we get (Anzer & Heinzel 2005)

$$r = \frac{1}{2}\left(1 + \text{e}^{-\tau}\right)r_{\text{b}}\tag{2}$$

and from this we obtain

$$\tau = -\ln\left(2\frac{r}{r_{\text{b}}} - 1\right).\tag{3}$$

This assumes that the coronal line emissivity is symmetrically distributed behind and in

front of the prominence (spherically symmetrical corona, the prominence lies in the plane of the sky).

In Heinzel et al. (2003) and Anzer & Heinzel (2005), the emissivity blocking was introduced to account for an additional reduction of the coronal brightness at the prominence position. Eq. (2) properly accounts for the fact that due to the blocking, the coronal background/foreground radiation is lowered compared to the case of a standard quiet corona. The blocking can be due to the prominence itself or due to the surrounding void (cavity) or due to both. This is schematically drawn in Fig. 5. In practice, we can proceed in two equivalent ways in order to account for the blocking effect.

First, we can use Eq. (2) (or its generalization for an asymmetric corona presented at the end of this subsection) with r defined as the ratio of the prominence intensity to that in the nearby corona. From XRT (no absorption) we can determine $r_{\rm b}$ as the ratio of the coronal intensity at a prominence position to that in the same coronal position for which r was determined. This is based on an assumption that XRT and the coronal-line emission which is absorbed (e.g. 195 Å line) have similar emissivity in the corona, at least in its quiet parts where the lower end of the XRT temperature response overlaps the Fe XII formation temperature – we will check this later using our observational data. However, even for relatively quiet corona, the solutions obtained from Eq. (3) will depend somewhat on the actual position in the corona outside the prominence for which r and $r_{\rm b}$ are computed, simply due to coronal inhomogeneities and noise in the data.

Another equivalent, but more efficient way is to again use the assumption of similarity between XRT and a coronal line emissivity and try to fit their corresponding intensity curves at coronal positions by e.g. the least-square method. Then $I_{\rm c}$ (or $I_{\rm c}'$) in both r and $r_{\rm b}$ will be identical and we can write

$$r = \frac{I_{\rm p}}{I_{\rm c}} = \frac{1}{2}\left(1 + {\rm e}^{-\tau}\right)\frac{I_{\rm cp}}{I_{\rm c}} \tag{4}$$

from which we simply get

$$r' = \frac{I_{\rm p}}{I_{\rm cp}} = \frac{1}{2}\left(1 + {\rm e}^{-\tau}\right) \tag{5}$$

and

$$\tau = -\ln\left(2\,r' - 1\right). \tag{6}$$

In our case, $I_{\rm cp}$ represents the XRT intensity *at the position of the prominence*, provided that in the corona *outside the prominence* both XRT and coronal-line intensities are the same (i.e. normalized to each other). In other words, XRT intensity serves here as a proxy of the coronal-line intensity and can be used at positions where the coronal line is normally

absorbed by the prominence body. This approach is also very illustrative. The coronal-line intensity at the prominence position shows the combined effect of absorption and blocking, while XRT shows directly the relative amount of blocking (note that this blocking naturally accounts for all kinds of emissivity depression of the coronal line, due to the presence of both prominence as well as the cavity). Their ratio at a prominence position then gives the amount of absorption as expressed in Eq. (5). Note that according to this formula, a minimum value of I_p is $1/2 \, I_{cp}$, in our case $1/2 \, I_{XRT}$. This corresponds to a saturation of the absorption for large τ. For such a saturated case, the solution for τ can still be obtained using an asymmetrical corona. In such a case we can write that the background radiation intensity I_b at the prominence position is that derived from XRT, multiplied by a factor $0 \leq \alpha \leq 1$. Then the foreground intensity I_f will be the $(1 - \alpha)$ fraction of the XRT intensity. For a symmetrical corona the parameter α is equal to $1/2$. With this we can write a generalized formula

$$ r' = \frac{I_p}{I_{cp}} = \alpha \left(\beta + e^{-\tau} \right) \tag{7} $$

where

$$ I_p = I_f + I_b \, e^{-\tau} \qquad I_{cp} = I_f + I_b \tag{8} $$

and $\beta = (1 - \alpha)/\alpha$. For the optical thickness we then get

$$ \tau = - \ln \left(\frac{r'}{\alpha} - \beta \right) . \tag{9} $$

A saturation of the absorption for large τ's leads to a limiting contrast equal to $1 - \alpha$ which in the case of a symmetric corona gives the value 0.5 . However, note that if we replace this true τ by an averaged value related to the spatial filling factor f (see the Appendix), we arrive at a limiting contrast equal to $1 - \alpha f$. This can be important for EUV lines which lie over the hydrogen Lyman continuum (CDS or SUMER lines like e.g. Mg X).

3.2. A comparison of multi-wavelength images – qualitative signatures of the absorption and blocking

The multi-wavelength images observed at the same time were coaligned using the pointing coordinates of the header with corrections due to mis-alignment (see section 2). We chose as a common time 13:19 UT when it is possible or the nearby observations. The EIS rasters the prominence between 13:34 and 13:54 UT. The multi-wavelength images are presented in Fig. 3. The EIS image is obtained after applying the response function of the TRACE 195 Å passband. In the Hα and CDS transition-region (PCTR) lines (not shown in the paper) we see the prominence in emission above the limb, with TRACE and EIS in

195 Å the prominence is dark. The prominence reaches an altitude of 50 arcsec (36 000 km) at its top. With XRT we see a huge bubble over the limb, 100 arcsec (73 000 km) wide and more than 200 arcsec long – this is the coronal cavity (void) around the prominence. At XRT wavelengths there is negligible absorption by resonance continua (they are transparent as shown recently by Anzer et al. (2007)) so that the prominence is not visible. In this case also the emissivity blocking due to the prominence itself (if the line-of-sight structure would be long enough) would cause no significant prominence visibility because the prominence is embedded into an already low-density (low-emissivity) cavity. The prominence that we observed was previously a long quiescent filament, very faint and very wide, lying along a parallel between 30 deg and 35 deg in the southern hemisphere. Due to its length and its position on the disk the cavity could be observed during three consecutive days from 2007 April 24 to 26. This picture is consistent with the geometrical considerations as presented by Fuller et al. (2008).

3.3.   XUV line and continuum intensity contrasts

The construction of the intensity cuts has been done as follows. Heights of the cuts above the solar surface were chosen so that they were passing close to the sets of points denoted 1, 2, 3 (cut No. 1); 5, 6, 7 (cut No. 2) and 9, 10 (cut No. 3) (see Fig. 4) where the Hα data from the MSDP and Ondřejov multi-channel spectrograph HSFA were reduced. We add a cut No. 0 closer to the limb. The positions of the cuts are shown in Fig. 3. In this figure the dashed line indicates an artificial limb of SOT which is not the true photospheric limb but we can use it as a reference. The dotted line then marks the bright Hα chromospheric limb. In the EIS and TRACE images the chromospheric limb is dark and is also marked by the same dotted line (the reason for this is that the Hα opacity is quite similar to that of resonance continua at 195   Å; this important behaviour is discussed later). Finally, we mark the XRT limb also by same dotted line, assuming that it is dark as in the 195   Å line, because of the chromospheric absorption of the background coronal X-ray radiation (Daw et al. 1995).

All four cuts were constructed to be parallel with the tangent to the limb and are 157 arcsec long (for the mean Sun-Earth distance). The zero cut was constructed at the height 8.7 arcsec above the SOT artificial limb (6 525 km), the cut No. 1 at the height 16 arcsec (11 800 km), the cut No. 2 at the height 30 arcsec (22 100 km) and the cut No. 3 at the height of 48 arcsec (35 300 km). For each instrument, all positions along the cuts were transformed from the solar-disk coordinate system expressed in arcsec into the image-centered coordinate system expressed in pixels. If the image coordinates of any position along the cut are not

integer numbers the weighted average of all adjacent pixels (both in x and y directions) to such position is taken. Weights were computed as follows: the closer to exact image position the pixel lies the higher weight this pixel has in averaging. For CDS the coordinates in arscsec should be transformed from the Sun-SOHO distance to Sun-Earth distance and then conversion to pixel position could be processed taking into account that the CDS prominence was rastered between 13:07 and 13:15 UT. Similar corrections have been made for EIS prominence region that was scanned between 13:34 UT and 13:54 UT.

To reduce noise the cut regions were constructed using one or two adjacent cuts on each side of each cut for all instrument observations so that they formed a box of similar widths: 2.5 arcsec for XRT, TRACE, EIS and 4.9 arcsec for CDS.

Fig. 6 shows the intensity depressions inside the prominence. The intensities of the corona outside of the prominence and the cavity have been overlaid in order to derive directly the ratios between the depression and the corona. There is a general agreement between EIS and TRACE cuts.

We examined the influence of spectral integration over the 195 Å bandpass of the TRACE instrument on the intensity depression at the prominence. We compared the depressions along all four cuts for three types of data: TRACE 195 Å data, intensities from the EIS observations integrated over the spectra in the range of the TRACE 195 Å bandpass taking into account also the response function of the TRACE 195 Å bandpass and intensities from the EIS observations integrated over the Fe XII line only. An example of the comparison for cut No. 1 is shown in Fig. 7. We found that the depressions in all three types of the data are very similar for all four cuts; this can be explained by the presence of several other coronal lines (except the Fe XII 195 Å line) in the spectrum in the range of the TRACE 195 Å bandpass (see Fig. 2) which have the same behaviour as the Fe XII line.

4. Opacities deduced from EUV contrasts

For all four cuts we used the novel procedure to determine τ as described at the end of Sec. 3.1. Along each cut we have selected regions which lie outside the Hα prominence (see curves of SOT intensities) and which do not contain active brightenings like that on cut No. 0 at position 35 (Fig. 6). This is considered to be a 'quiet' corona for which we believe that the X-ray emissivity is similar to that of the Fe XII 195 Å line. We therefore try to fit both XRT and TRACE intensity curves using the least-square technique. The results are shown in Fig. 6, where a reasonably good fit was found for all four cuts, even in regions which correspond to the coronal cavity (see e.g. cuts No. 2 and No. 3 at positions 0 to 50).

On the other hand, bright active regions above the limb (namely in cut No. 0) are much brighter in X-rays than in the Fe XII line, which indicates a large temperature difference in corona. Significantly reduced FeXII emission at this position is not due to the absorption because there is no cool structure visible in the SOT data. Note that XRT intensity at the prominence position, compared to that in the external corona, gives the emissivity blocking due to both the prominence and cavity. On the other hand, TRACE or EIS at the same position show the combined effect of absorption and blocking. The difference between XRT and TRACE/EIS is then entirely due to the absorption – see plots in Fig. 6 at the positions of SOT Hα emission.

Finally, we have also tried to fit EIS intensity curves to those of TRACE at the same quiet-corona positions. This resulted in somewhat lower EIS intensities at the prominence positions as compared to TRACE. As mentioned above, the integrated EIS spectrum over the TRACE 195 Å channel (see Fig. 2) gives almost identical results as for Fe XII 195 Å line alone and this indicates that both instruments should give the same intensity in this channel. However, TRACE is not a spectrograph, the spatial resolution of both instruments is not the same and, moreover, the EIS data were obtained about half an hour later than the TRACE data (the prominence fine structure is evolving in time and we can check the relative brightness of SOT Hα at different times). To derive τ at 195 Å, we first used the assumption of a symmetrical corona and computed the optical thickness at all prominence positions using Eq. (9) with $\alpha = 1/2$. The result is shown in Fig. 8, for all four cuts. We see that τ at the darkest points of TRACE in cut No. 2 can reach values around 4, while EIS gives generally larger values, although in the case of cut No. 2, EIS data give no solution in many places, i.e. the EIS intensity is lower than $1/2$ of the XRT. As a next step, we assumed that $I_{\rm b}$ is larger than $I_{\rm f}$, which seems to be consistent with our (rather noisy) data from CDS in Mg X line. The hydrogen Lyman continuum at the wavelength position of this line (625 Å) is optically thick in cases when τ_{195} is around one or larger. This then means that the absorption of the background coronal radiation in Mg X line is saturated (see also Kucera et al. 1998 or Schmieder et al. 1999) and we actually see, at the darkest prominence places, only the foreground coronal radiation (provided that the filling factor f is equal to one; otherwise the limiting contrast is equal to $1 - \alpha f$ as was shown above). From our Mg X cuts we generally see that the intensity at the darkest prominence positions is in several cases lower than $1/2$ of the fitted XRT intensity. Therefore we tested our solutions with $\alpha = 0.7$. The results obtained with Eq. (9) are shown in Fig. 9. In this figure all points along the cut No. 2 now have a reasonable solution for EIS data and, moreover, τ computed for both EIS and TRACE are now naturally lower than for a symmetrical case. As we will see later, this corresponds better to values of $\tau_{\rm o}({\rm H}\alpha)$ discussed in the next section. We give the values of τ_{195} at selected points detected by MSDP in Table 1.

One distinct feature is the very bright point in cut No. 0 around position 35, which shows a strong brightening in X-rays. Inspection of TRACE or EIS images indicates a very sharp absorption edge which we interpret as due to the absorption of the radiation from a strong background source, with a negligible foreground contribution. In this case our parameter α may reach unity and thus the values of τ in Fig. 9 computed for $\alpha = 0.7$, might be overestimated at the position of this brightening.

In Fig. 6 we can also see a relatively good anticorrelation between TRACE intensities and the SOT Hα brightness. For example in cut No. 3 we notice two narrower minima in TRACE curve (roughly at position 58 and 68) and one broader minimum around position 80 which correspond to Hα maxima in the SOT curve. This is further reflected in Figs. 8 and 9, where τ_{195} correlates quite well with the Hα brightness. However, the correlation of Hα with EIS intensity curves is less convincing.

5. Opacity in the Hα line

5.1. The method

As demonstrated by Heinzel et al. (2001) and later by Anzer & Heinzel (2005), there exists a close correlation between the opacity of the hydrogen Lyman continuum and that of the Hα line. Therefore, the knowledge of the Hα line opacity or the line-center optical thickness of the prominence $\tau_{\mathrm{o}}(\mathrm{H}\alpha)$ gives us immediately an estimate of the Lyman-continuum absorption and, using the results of Anzer & Heinzel (2005), also the absorption by helium resonance continua. $\tau_{\mathrm{o}}(\mathrm{H}\alpha)$ is well correlated with the integrated intensity of Hα as follows from theoretical non-LTE models of Gouttebroze et al. (1993). This correlation is shown in Heinzel et al. (1994) (see their Fig. 5), where one can notice a rather weak dependence on the temperature. To obtain the integrated line intensity, we used both MSDP as well as HSFA observations. Along the cuts analyzed in the previous section we have selected several points in which the Hα line intensity was determined – see Fig. 4 where these points are marked within the SOT image taken almost at the same time.

5.2. Calibration of Hα ground-based observations

The normalization of the intensities of the MSDP was done as follows. The intensities of the observed profiles I_λ are automatically normalized to the local continuum $I_\lambda/(I_{\mathrm{c,loc}})_{\mathrm{obs}}$. In order to compare the observed intensities with those calculated theoretically, we renormalize the intensities to the continuum at disk center I_λ/I_{c}. The continuum at disk center in the

wavelength region close to the Hα line has intensity $I_c = 4.077 \times 10^{-5}$ erg cm^{-2} s^{-1} sr^{-1} Hz^{-1}. To renormalize we must apply two corrections : (i) one due to the limb darkening. The reference profiles are measured on the disk near the limb at $\sin\theta = 0.98$. It reduced the intensity by a factor 0.547, (ii) the central intensity is no longer equal to 16 % of the intensity of the continuum but is equal to 22.6 %.

The normalization of the intensities of the HSFA was done as follows. The Hα spectra were corrected for dark frames and flat-field in a standard way. Then the dispersion relation was found comparing the positions of about 20 spectral lines in the field of view of the spectral strip close to the Hα line with those in the solar spectral atlas. Relative-intensity profiles of the solar limb were compared to the corresponding Hα intensity profiles of David (1961) to find a factor converting them into local continuum values. Then, using relations of Allen (1985) for the center-limb darkening, the conversion to intensity units expressed in erg sec^{-1} cm^{-2} sr^{-1} Å^{-1} was carried out. Scattered light was subtracted and the Hα line profiles in selected places of the prominence were integrated to obtain the integrated intensities.

5.3. Results

In Table 1 we present the Hα integrated intensities at points marked in Fig 4 (note that the HSFA data calibration was not performed at all these points but only in the brightest ones). We see that the results from both GBOs are quite compatible, the differences being typically less than 20 % (due to calibration, scattered light, instrumental differences, etc.). These intensities can be directly used to obtain the values of τ_o(Hα), i.e. the line-center optical thickness of the prominence along the line of sight, at selected points. As already mentioned, the temperature dependence is rather weak and here we used $T=8\,000$ K as a typical temperature of the Hα forming regions. The resulting τ_o(Hα) is given in Table 1.

6. Optical thickness of the hydrogen Lyman continuum

Using TRACE/EIS, CDS and Hα data we are able to derive τ_{912}.

6.1. TRACE, EIS and XRT

The optical thickness at 195 Å was obtained in section 3. To convert this τ to that at the head of the hydrogen Lyman continuum, we use the approximate relation of Anzer &

Heinzel (2005)

$$\tau_{195}/\tau_{912} \simeq 12.09 \times 10^{-3} + 1.93 \times 10^{-2} f(i) \,, \tag{10}$$

where $f(i) = 1/(1 - i)$ depends on the mean hydrogen ionization degree $i = N_{\mathrm{p}}/N_{\mathrm{H}}$ with N_{p} and N_{H} being, respectively, the proton and total hydrogen column density. Note that this equation was derived assuming a relative helium abundance $r_{\mathrm{He}} = 0.1$ and a negligible population of the He III state (which seems to be reasonable inside the cool parts of the absorbing prominence medium). The great advantage of this formula is that it does not depend on He II population - this follows from a rough equality between He I and He II continuum opacity at 195 Å (Mein et al. 2001; Anzer & Heinzel 2005). If He III has non-negligible abundance in the cool parts of a prominence, the function $f(i)$ in Eq. (10) is replaced by $f(i, j_2) = (1 - j_2)/(1 - i)$. Non-zero j_2 clearly lowers the opacity at 195 Å and the corresponding τ becomes comparable to $\tau_{\mathrm{o}}(\mathrm{H}\alpha)$.

6.2.   CDS and XRT

The most reliable coronal CDS data obtained for this prominence are those for the Mg X line at 625 Å where the signal-to-noise ratio is at a reasonable level. Ca X and Si XII data are much noisier. At the wavelength position of the Mg X line, the optical thickness of the hydrogen Lyman continuum (only this continuum matters) is computed using Eq. (3) which takes into account the emissivity blocking contrast derived from XRT images. At selected points marked in Fig. 4, the computed optical thickness is given in Table 2. However, these values of τ are too low and inconsistent with TRACE or EIS results. We can compare $\tau_{912} = 2.5\,\tau_{625}$ with τ_{912} given in Table 3 for values of $\tau_{\mathrm{o}}(\mathrm{H}\alpha)$ and τ_{195} derived from our optical and TRACE data. The difference is large, in most cases reaching almost one order of magnitude. Therefore, the CDS data cannot be used to derive τ_{912} directly, although this method would be the most straightforward. The following aspects of the problem are worth discussing. For large τ_{912} which follow from optical and TRACE/EIS data the absorption of Mg X would be saturated - such saturation is frequently met in the data, as noted by Kucera et al. (1998) and Schmieder et al. (1999). However, in cases where the prominence is less optically thick in the 195 Å channel, the Mg X line can be used to derive reliable values of τ_{912} provided that this line is observed with a favorable signal/noise ratio (see the results from SOHO/SUMER observations presented by Anzer et al. (2007)).

Table 1: Integrated intensities E of the Hα line as determined from MSDP and HSFA observations in positions indicated in Fig. 4. E is in units $10^5\,\mathrm{erg\,cm^{-2}\,s^{-1}\,sr^{-1}}$. We also indicate the difference in % between the two observations. The line center optical thickness was finally derived using the MSDP data.

point	E(MSDP)	E(HSFA)	diff [%]	τ_0
1	1.11	1.07	4	1.3
2	0.98	1.17	16	1.2
3	0.23			0.2
4	0.77			0.8
5	0.94	1.27	26	1.1
6	1.17	1.36	14	1.4
7	1.11	0.94	18	1.3
8	0.58			0.6
9	0.47			0.5
10	1.16	1.31	11	1.4
11	0.42			0.4
12	0.11			0.1

Table 2: Optical thickness at 195 Å and at Mg X 625 Å computed from EUV absorption by resonance continua and τ_o(Hα) obtained from the Hα integrated intensity. We give two values for EUV absorption, for symmetrical corona and for $\alpha = 0.7$ (values in parentheses).

point	TRACE	EIS	CDS	Hα
1	2.0 (0.95)	3.0 (1.12)	-	1.3
2	1.9 (0.95)	2.2 (1.0)	-	1.2
3	0.25 (0.17)	0.55 (0.37)	-	0.2
5	1.0 (0.58)	- (1.65)	0.7	1.1
6	1.5 (0.8)	3.5 (1.2)	2.2	1.4
7	1.6 (0.83)	2.2 (1.0)	-	1.3
9	0.6 (0.4)	1.1 (0.65)	1.1	0.5
10	0.85 (0.53)	2.5 (1.08)	1.7	1.4

7. Discussion of results

We see from Table 3 that $\tau_{\mathrm{o}}(H\alpha)$ obtained from GBO data is quite similar to τ_{195}. This result was already obtained in Mein et al. (2001) and Schmieder et al. (2004) using TRACE and Hα data for, respectively, an arch filament system and a filament, where a similar fine structure was seen at both wavelengths. The theoretical grounds of this important correlation were discussed by Anzer & Heinzel (2005) (and shown in Table 3). However, in our present observations these values are not consistent with the optical thickness of the hydrogen Lyman continuum derived here from CDS lines. Considering the Mg X line (other lines are more noisy), we have $\tau_{912} = 2.5\,\tau_{625}$. This gives values of τ_{912} which are much lower than the theoretical values shown in Table 3. A similar or even worse situation arises for Ca X and Si XII lines at points 1 and 2.

7.1. Spatial averaging of optical and EUV intensities

Assuming that the CDS data are accurate enough and have been correctly reduced/calibrated, the only explanation we can suggest here is the influence of a spatial averaging. This explanation is possible thanks to information from high-resolution images taken by SOT. Although we could not use SOT images directly to obtain $\tau_{\mathrm{o}}(H\alpha)$ (only the line-center intensity was detected and this was not radiometrically calibrated), we see from them that at spatial resolution $0.2-0.3$ arcsec, TRACE, CDS, and also GBO Hα contain many fine-structure elements within the spatial box over which the intensities have been averaged. Actually TRACE has a spatial resolution around 1 arcsec, CDS 4 arcsec and GBO Hα also several arcsec because of the seeing, moreover, we have integrated over several pixels to obtain our cuts. In the Appendix we demonstrate that in the case of EUV absorption, the mean τ is related to the

Table 3: Theoretical optical thicknesses and hydrogen ionization degree i according to Anzer & Heinzel (2005). Upper line of each table row corresponds to temperature $T=6\,000$ K, lower one to $T=8\,000$ K.

$\tau_{\mathrm{o}}(H\alpha)$	τ_{195}	τ_{912}	i
0.5	0.9	13	0.66
	1.0	13	0.70
1.0	1.7	30	0.56
	1.6	25	0.62
2.0	3.2	70	0.43
	2.8	50	0.56

τ of individual fine structures in a *non-linear* way, while for Hα this relation is linear. As follows from Fig. 10, the low values of τ obtained from CDS lines can be related to a specific value of the filling factor. The saturation of curves which correspond to non-linear averaging demonstrates that by increasing the true τ, the mean τ can only reach the value $-\ln(1-f)$ (in case of a symmetric corona and under the assumptions used in the Appendix). Taking the mean value of the derived τ_{625} from Table 2, which is about 1.6, we see that this is the saturated value for $f = 0.8$. Note that this value of f together with $\alpha = 0.7$ assumed above for the case of a non-symmetric corona leads to a limiting contrast in the Mg X line equal to $1 - \alpha f = 0.44$, which still indicates a saturation (lowering f requires larger values of α).

The effect of low spatial resolution due to seeing is much less critical for the Hα line as we can also see from Fig. 10 where the averaged τ is related to the true one by straight dashed lines. Also τ_{195} is not affected as much by the spatial resolution and data averaging of TRACE, first because TRACE has better resolution than CDS, and second because τ_{195} is around one and thus the non-linear averaging is not saturated. We see that for all values of a given f, the true τ_{195} is always larger than $\tau_{\mathrm{o}}(\mathrm{H}\alpha)$, provided that the mean values are comparable as in our data. This is consistent with theoretical results shown in Table 3 where the results for two temperatures are similar. Our values of $\tau_{\mathrm{o}}(\mathrm{H}\alpha)$ between 1 and 2 are consistent with a hydrogen ionization degree i between 0.4 and 0.6. This involves the central cool parts of the prominence, emitting in the Hα line and absorbing coronal radiation in EUV resonance continua of hydrogen and helium. Our results also indicate that the ionization degree of singly ionized helium j_2 is small (for our analysis we assumed $j_2 = 0$). This is consistent with the results of non-LTE prominence modeling of Labrosse & Gouttebroze (2004) who also found a negligible abundance of He III in central parts of the prominence slab.

7.2. Hydrogen column density

Using τ_{195} obtained from our observations, one can directly estimate the hydrogen column density N_{H} at a given prominence position. Assuming again that the He I and He II continuum cross-sections are the same, we get from Eq. (1)

$$N_{\mathrm{H}} = \frac{\tau_{195}}{(1-i)\sigma_{\mathrm{H}}^{195} + r_{\mathrm{He}}\sigma_{\mathrm{He}}^{195}} \tag{11}$$

and using the data from Anzer & Heinzel (2005) we obtain

$$N_{\mathrm{H}} = \frac{10^{19}}{2 - 0.8i} \tau_{195} \tag{12}$$

which for i=0.5 gives simply $N_{\mathrm{H}} = 1.6 \times 10^{19} \tau_{195}$. With the values of τ_{195} shown in Fig. 8 we find that N_{H} is roughly in the range $1 - 5 \times 10^{19}$ cm^{-2}. These hydrogen column densities are quite reasonable, comparable to previously results, such as those obtained by Gilbert et al. (2005, 2006) or Anzer et al. (2007). For a hydrogen density of the order of 10^{11} cm^{-3} which is characteristic of quiescent prominences at temperatures $6\,000 - 8\,000\,\mathrm{K}$, we get an effective prominence thickness around $1 - 5 \times 10^3$ km, which is a quite reasonable value. A great advantage of this method is that the dominant opacity of helium resonance continua does not depend on the ratio He II/He I (j_1 in our notation) but only on total helium density (assuming that He III density is negligible in cool parts of a prominence, see non-LTE computations of Labrosse & Gouttebroze (2004)). Our solutions thus only assume a knowledge of the hydrogen ionization degree i, but this varies, for a given temperature, within a rather narrow range of values around 0.5 (see Table 3). Note that Gilbert et al. (2005) used a different source of opacity data for He I from which the He I continuum opacity is a factor 1.5 larger than that of He II (their He II opacity is the same as ours since it simply follows from the hydrogen-like atomic model). This difference, larger than in our case, led the authors not to assume the equality of both opacities and this, in turn, requires knowledge of j_1. Using the VAL model of the chromosphere (Vernazza et al. 1981), Gilbert et al. (2005) assumed $0.005 \leq j_1 \leq 0.14$, generally lower than values given by Labrosse & Gouttebroze (2004)).

8. Conclusions

In this paper we have used the opportunity to combine multi-wavelength prominence data for a detailed quantitative analysis of the EUV coronal line absorption and blocking. We were fortunate to observe a prominence which shows all of the major aspects of these mechanisms, such as the coronal darkening at the prominence position and the cavity around the prominence. A coordinated Hinode-SUMER campaign allowed us to obtain the multi-wavelength data from several space instruments and GBOs. Hinode/XRT allows us to determine the blocking much better than with SXT (used in Anzer et al. 2007) and we have suggested here a modified method which directly uses the XRT intensity curve to account for the emissivity blocking. This study presents the first simultaneous observations in the 195 Å line (channel) by Hinode/EIS and TRACE with Hα. They confirm, for the prominence situation, that the helium resonance-continua opacity is similar at 195 Å and in Hα, a result previously obtained theoretically by Anzer & Heinzel (2005) and observationally for

filaments in Schmieder et al. (2004). This result was then used in the analysis of the Hα filament and its channel by Dudík et al. (2008). These opacities are now shown to be consistent with theoretical non-LTE models of prominences, namely the computation of the Hα and hydrogen Lyman-continuum optical thickness. 195 Å opacities empirically derived here can serve as constraints for non-LTE models of He line and continua formation (Labrosse & Gouttebroze 2004).

Opacity in the hydrogen Lyman continuum could not, however, be determined properly using the Mg X line observed by CDS. This is probably because of the low spatial resolution of CDS. We demonstrate here for the first time the importance of high spatial resolution for correct determination of EUV opacities using the absorption/blocking model for prominences. The basic idea of a non-linear averaging is developed in the Appendix. The importance of this effect depends on the filling factor which corresponds to the respective EUV data and also on the continuum opacity which is wavelength dependent.

Our results obtained with TRACE seem to be more consistent with Hα observations than are the data from EIS. EIS as the next-generation EUV spectrometer is supposed to provide excellent data and thus we think that the problem with our observations is mainly due to the unfortunate circumstance that the Hinode satellite passed into an eclipse period exactly at time of the prominence rastering. The way we have corrected EIS data for this effect may not be optimal, although some of our tests do indicate that no significant error was introduced. Another reason could be the time difference between our TRACE and EIS observations – from the SOT prominence movie we clearly see a significant temporal evolution of the prominence fine structure.

Another siginificant result is the determination of the hydrogen column density, found to be in the range $1-5 \times 10^{19}\,\mathrm{cm}^{-2}$, fully consistent with other studies. The technique for determination of prominence column masses based on the analysis of coronal-line depressions is promising for studies of prominence eruptions and mass loading of related CMEs (Gilbert et al. 2006).

In conclusion, we suggest performing future multi-wavelength observations using more coronal lines by EIS (including those above 228 Å), calibrated Hα intensities from SOT, and XRT, which has proven to provide a useful proxy of coronal-line intensities at the place of an absorbing prominence. Moreover, one can also consider simultaneous SUMER observations in selected coronal lines below as well as above 912 Å as discussed in Anzer et al. (2007). We will further develop our non-LTE prominence models to be consistent with the opacities and column densities empirically derived from these multi-wavelength prominence observations.

9. Acknowledgment

10. Appendix

Let us assume that the SOT spatial resolution is about 0.3 arcsec, while the intensities measured with EUV space instruments (TRACE, SOHO/CDS, SOT/EIS) are averaged over much larger boxes. If the fine-structure elements have a typical size comparable to SOT resolution (see part of the SOT image with fine structures), we will have a large number of them within the resolution box of EUV space instruments - this can be characterized by a spatial *filling factor f.* Let us further assume, for simplicity reasons, that only two different intensities are present for such elements, I_1 and I_2 which correspond to f and $(1 - f)$ filling factors, respectively. For the EUV absorption model we then write

$$I_1 = \frac{1}{2}\left(1 + e^{-\tau_1}\right) I_{cp} \qquad I_2 = \frac{1}{2}\left(1 + e^{-\tau_2}\right) I_{cp} \tag{13}$$

Spatially averaged intensity will be equal to

$$I = f\, I_1 + (1 - f)\, I_2 \tag{14}$$

and in terms of averaged τ

$$I = \frac{1}{2}\left(1 + e^{-\tau}\right) I_{cp} \tag{15}$$

Combining these equations we obtain for mean τ

$$\tau = -\ln\left[f\,\mathrm{e}^{-\tau_1} + (1-f)\,\mathrm{e}^{-\tau_2}\right]\,. \tag{16}$$

This averaging of τ using the EUV intensities is *non-linear* due to absorption terms $\mathrm{e}^{-\tau}$.

Hα intensities as measured by MSDP or HSFA are also averaged over a substantially large box (mainly due to the seeing effect), but in this case the averaging of τ is *linear*, by nature quite different from that for EUV. In case of Hα, the intensity is converted to τ using the linear relation $\log I - \log I_0 = \gamma \log \tau$ (see Heinzel et al. 1994), which simply gives $I = I_0 \tau^\gamma$. With this and with Eq. (14) we get

$$\tau = [f\tau_1^\gamma + (1-f)\tau_2^\gamma]^{1/\gamma}\,. \tag{17}$$

Finally, assuming the simplest case when we have a fraction f of fine-structure elements with intensity I_1 and $(1-f)$ of coronal features between them (which have $\tau_2 = 0$), we get for the EUV case

$$\tau = -\ln\left[f\mathrm{e}^{-\tau_1} + (1-f)\right] \tag{18}$$

while for Hα we have (taking $\gamma = 1$)

$$\tau = f\tau_1\,. \tag{19}$$

Note that for Hα line-center τ larger than one, the parameter γ starts to deviate from unity (e.g. Heinzel et al. (1994)).

In Fig. 10 we show the behaviour of these two types of the spatial averaging, for various values of the filling factor. It is important to realize that since the averaged optical thickness depends on the actual τ_1 of the hydrogen and helium EUV continua (i.e. the optical thickness of the hydrogen and helium resonance continua at the wavelength of the measured EUV line), the behaviour of the non-linear averaging is wavelength-dependent. For EUV lines which are absorbed at larger τ_1 (closer to the continuum head) the averaging effect will be more important.

REFERENCES

Allen, E. W. 1985, Astrophysical Quantities (the Athlone Press, London and Dover, New Hampshire), Third Edition

Anzer, U., & Heinzel, P. 2005, ApJ, 622, 714

Anzer, U., Heinzel, P., & Fárnik, F. 2007, Sol. Phys., 242, 43

Berger, T. E., et al. 2008, ApJ, in press

Culhane, J. L., et al. 2007, Sol. Phys., 243, 19

David, K.-H. 1961, Zeitschrift fur Astrophysik, 53, 37

Daw, A., Deluca, E. E., & Golub, L. 1995, ApJ, 453, 929

Dere, K. P., Landi, E., Mason, H. E., Monsignori Fossi, B. C., & Young, P. R. 1997, A&AS, 125, 149

Dudík, J., Aulanier, G., Schmieder, B., Bommier, V., & Roudier, T. 2008, Sol. Phys., in press

Engvold, O., Jakobsson, H., Tandberg-Hanssen, E., Gurman, J. B., & Moses, D. 2001, Sol. Phys., 202, 293

Fuller, J., Gibson, S. E., de Toma, G., & Fan, Y. 2008, ApJ, in press

Gilbert, H. R., Falco, L. E., Holzer, T. E., & MacQueen, R. M. 2006, ApJ, 641, 606

Gilbert, H. R., Holzer, T. E., & MacQueen, R. M. 2005, ApJ, 618, 524

Golub, L., et al. 1999, Physics of Plasmas, 6, 2205

Golub, L., et al. 2007, Sol. Phys., 243, 63

Gouttebroze, P., Heinzel, P., & Vial, J. C. 1993, A&AS, 99, 513

Gunár, S., Heinzel, P., Schmieder, B., Schwartz, P., & Anzer, U. 2007, A&A, 472, 929

Handy, B. N., et al. 1999, Sol. Phys., 187, 229

Handy, B. N., Bruner, M. E., Tarbell, T. D., Title, A. M., Wolfson, C. J., Laforge, M. J., & Oliver, J. J. 1998, Sol. Phys., 183, 29

Harrison, R. A., et al. 1995, Sol. Phys., 162, 233

Heinzel, P. 2007a, in Astronomical Society of the Pacific Conference Series, Vol. 370, Solar and Stellar Physics Through Eclipses, ed. O. Demircan, S. O. Selam, & B. Albayrak, 46

Heinzel, P. 2007b, in Astronomical Society of the Pacific Conference Series, Vol. 368, The Physics of Chromospheric Plasmas, ed. P. Heinzel, I. Dorotovič, & R. J. Rutten, 271

Heinzel, P., Anzer, U., & Gunár, S. 2005, A&A, 442, 331

Heinzel, P., Anzer, U., & Schmieder, B. 2003, Sol. Phys., 216, 159

Heinzel, P., Gouttebroze, P., & Vial, J.-C. 1994, A&A, 292, 656

Heinzel, P., Schmieder, B., & Tziotziou, K. 2001, ApJ, 561, L223

Kosugi, T., et al. 2007, Sol. Phys., 243, 3

Kotrč, P. 2007, in Astronomical Society of the Pacific Conference Series, Vol. 368, The Physics of Chromospheric Plasmas, ed. P. Heinzel, I. Dorotovič, & R. J. Rutten, 559

Kucera, T. A., Andretta, V., & Poland, A. I. 1998, Sol. Phys., 183, 107

Kucera, T. A., & Landi, E. 2008, ApJ, 673, 611

Labrosse, N., & Gouttebroze, P. 2004, ApJ, 617, 614

Labrosse, N., Schmieder, B., Heinzel, P., Gunár, S., & Watanabe, T. 2008, A&A, in preparation

Landi, E., & Phillips, K. J. H. 2006, ApJS, 166, 421

Mein, N., Schmieder, B., DeLuca, E. E., Heinzel, P., Mein, P., Malherbe, J. M., & Staiger, J. 2001, ApJ, 556, 438

Mein, P. 1977, Sol. Phys., 54, 45

—. 1991, A&A, 248, 669

Schmieder, B., Kotrč, P., Heinzel, P., Kucera, T., & Andretta, V. 1999, in ESA Special Publication, Vol. 448, Magnetic Fields and Solar Processes, ed. A. Wilson & et al., 439

Schmieder, B., Lin, Y., Heinzel, P., & Schwartz, P. 2004, Sol. Phys., 221, 297

Schmieder, B., Tziotziou, K., & Heinzel, P. 2003, A&A, 401, 361

Schwartz, P., Heinzel, P., Anzer, U., & Schmieder, B. 2004, A&A, 421, 323

Suematsu, Y., et al. 2008, Sol. Phys., in press

Vernazza, J. E., Avrett, E. H., & Loeser, R. 1981, ApJS, 45, 635
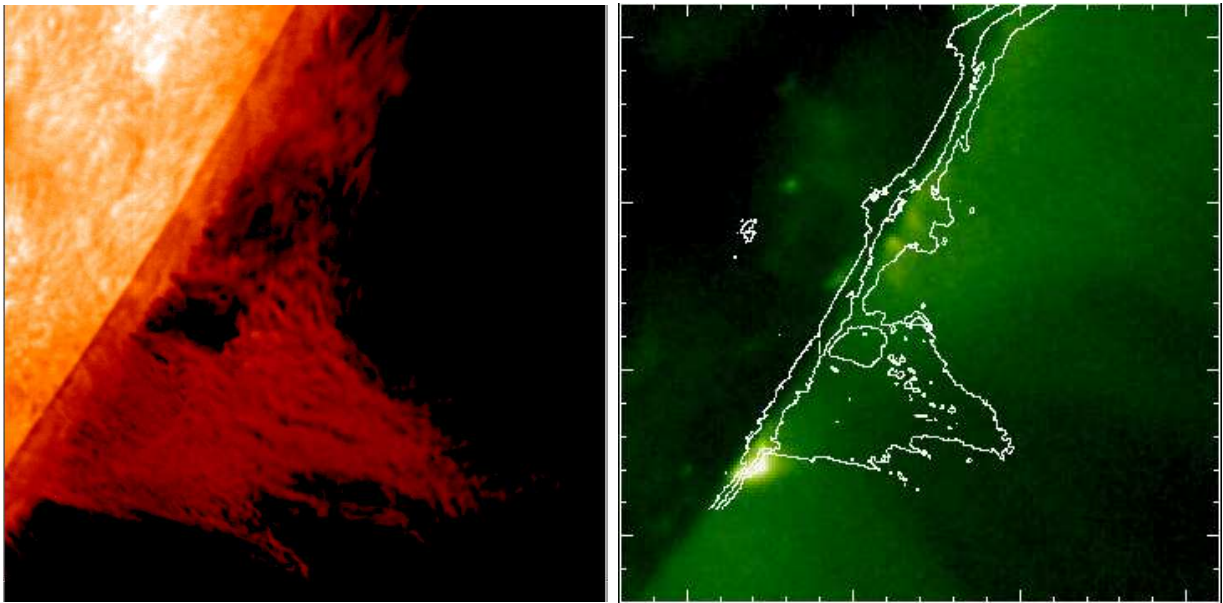
Wilhelm, K., et al. 1995, Sol. Phys., 162, 189

Fig. 1.— Hα prominence (left panel) observed on 2007 April 25 at 13:19 UT by Hinode/SOT (cut-off 80 arcsec × 80 arcsec) and Hinode/XRT image (right panel) overlaid by contours of the Hα prominence (20, 30, 40 % of the intensity maximum). Tick unit is 10 arcsec. A large coronal cavity is seen over the Hα prominence.
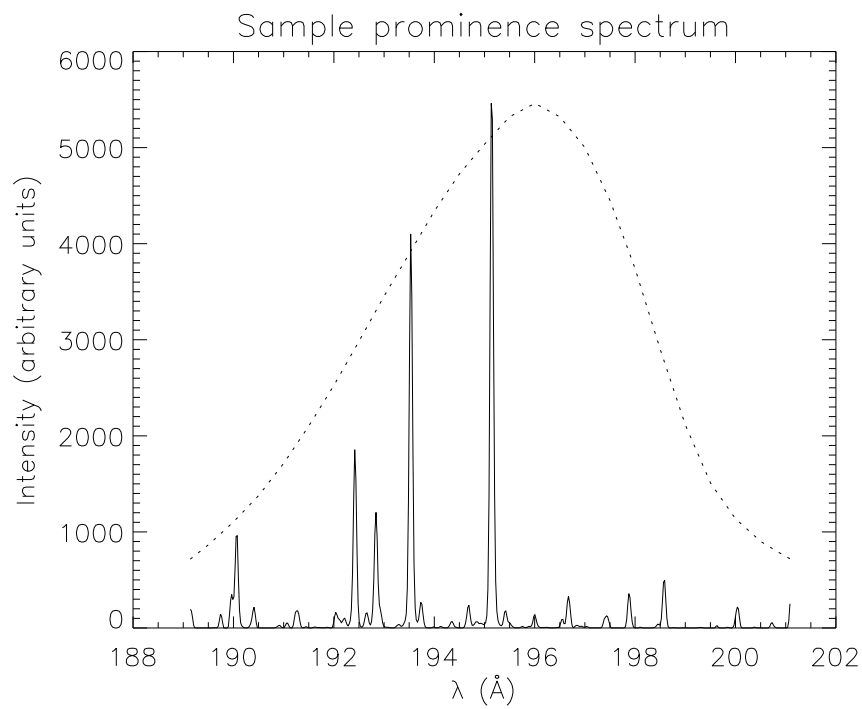
Fig. 2.— EIS spectrum around the Fe XII 195 Å line (full line) and the response function of the TRACE 195 Å bandpass (dotted line).
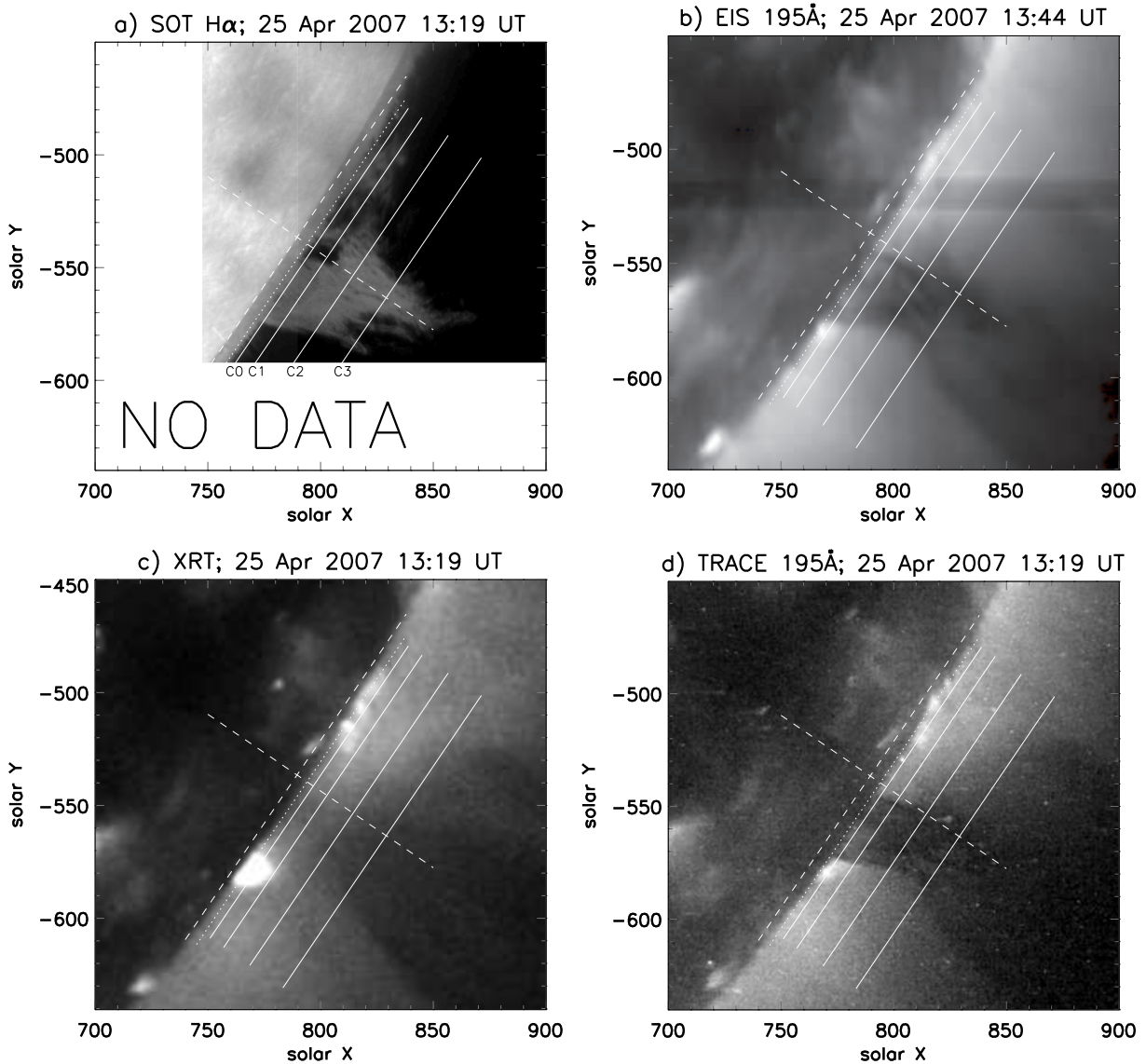
Fig. 3.— Multi-wavelength images obtained with SOT in Hα shown in the panel **a)**, with EIS in the TRACE 195 Å bandpass shown in the panel **b)**, with XRT shown in the panel **c)** and with TRACE in 195 Å bandpass shown in the panel **d)**. The cuts No. 0 – No. 3 (marked with the full white lines) are overlaid and are labelled as C0 – C3 in the SOT image. Dotted and dashed lines represent the chromospheric and an artificial SOT limbs, respectively. The prominence was observed at 13:19 UT by all the instruments except of EIS spectrograph which rastered it between 13:34 and 13:54 UT. The EIS image is constructed using the response function of TRACE 195 Å bandpass.
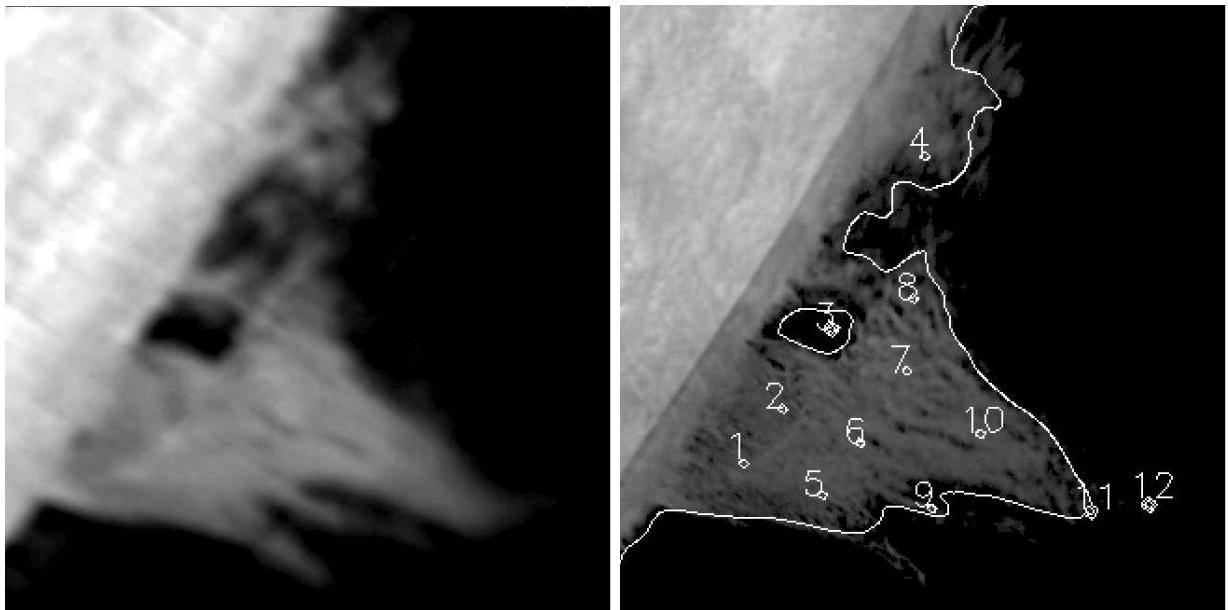
Fig. 4.— Prominence observed in the Hα line center by the MSDP spectrograph (left panel) and by Hinode/SOT (right panel) on 2007 April 25 at 13:19 UT. On the image of SOT we have overlaid the contour of the MSDP observation and indicated points where the opacity has been computed using MSDP and HSFA spectra.
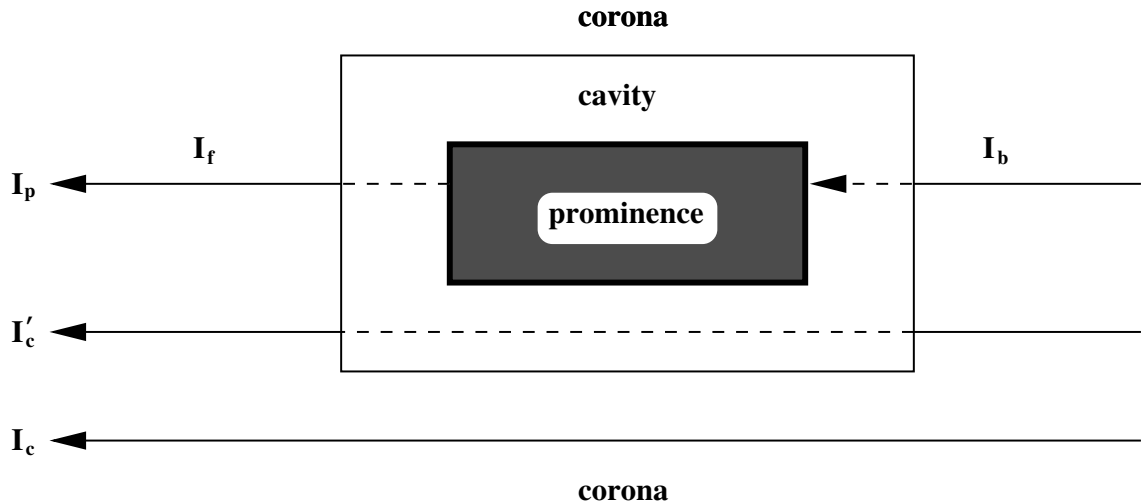
Fig. 5.— Absorption and emissivity blocking scheme. I_c is the coronal intensity outside the prominence. When the line of sight is passing through the cavity surrounding the prominence, I'_c is the intensity of coronal radiation lowered due to the presence of a cavity. In the case of line of sight passing through the prominence, coronal EUV lines with wavelength below $912\,\text{Å}$ are absorbed by the resonance continua of hydrogen and helium in a cool prominence. There is a depression of the coronal brightness due to cavity plus lack of coronal emission in the prominence volume and the absorption of background radiation I_b. I_f is the intensity of radiation emitted by the corona and void in front of the prominence. I_p is the intensity observed at the prominence location. In case of XRT observations there is no absorption by the prominence, only a depression of coronal emission due to the cavity plus a lack of coronal emission in the prominence volume. For this case we denoted I_p as I_{cp} in the text and in in the equations.
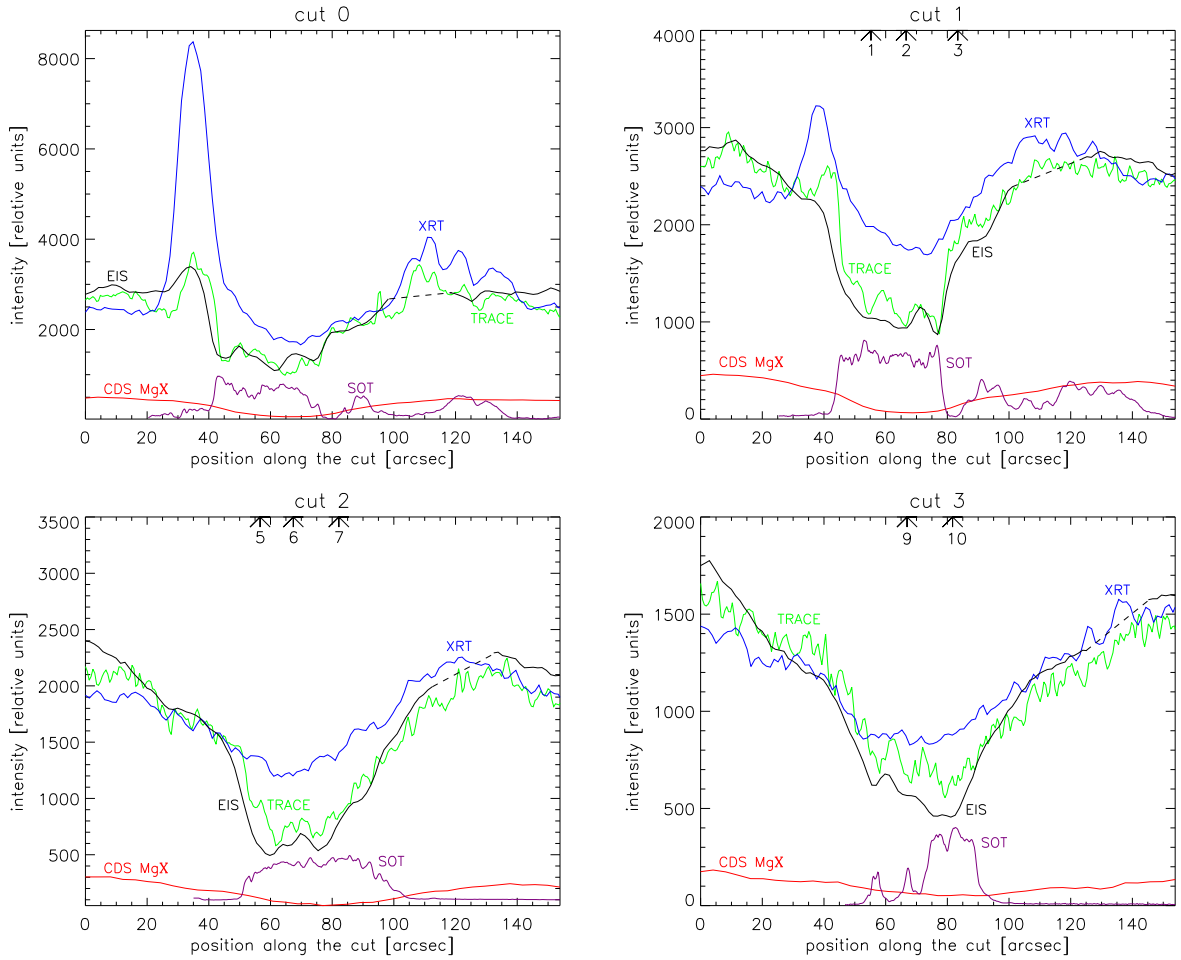
Fig. 6.— Cuts through the prominence at different altitudes over the limb. Positions of the cuts are shown in Fig. 3. Intensities of XRT, EIS 195 Å, TRACE 195 Å and CDS Mg X are in relative units. Intensities of Hα from SOT observations were rescaled and placed to the bottom of the plots. The EIS data plotted with dashed lines mark sections where the cuts are crossing the horizontal dark stripe. Arrows at the top of the plots mark the positions of the points shown in Fig. 4.
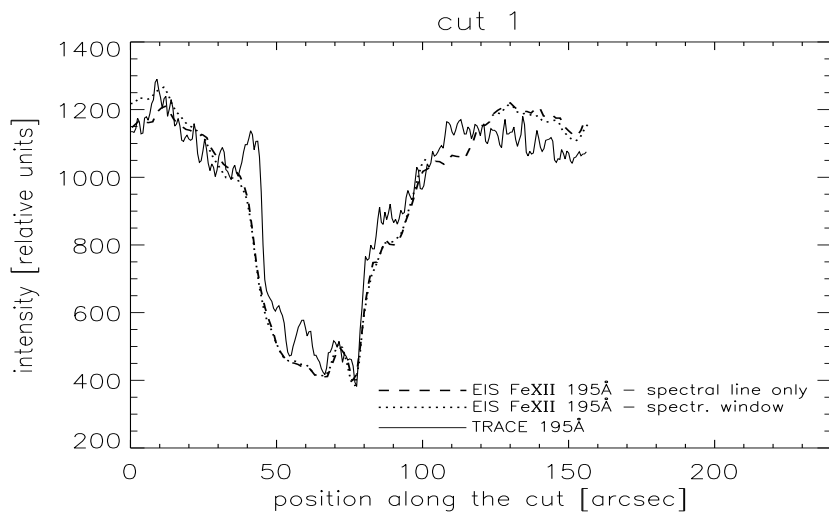
Fig. 7.— Comparison of data from cut No. 1 observed by EIS in the FeXII 195 Å line only, by EIS integrated over the TRACE 195 Å bandpass and by TRACE in its 195 Å bandpass. Integrated EIS data are interrupted between positions 101 and 124 arcsec along the cut because the cut crosses the dark horizontal stripe there (see panel b) in Fig. 3) where data are not reliable.
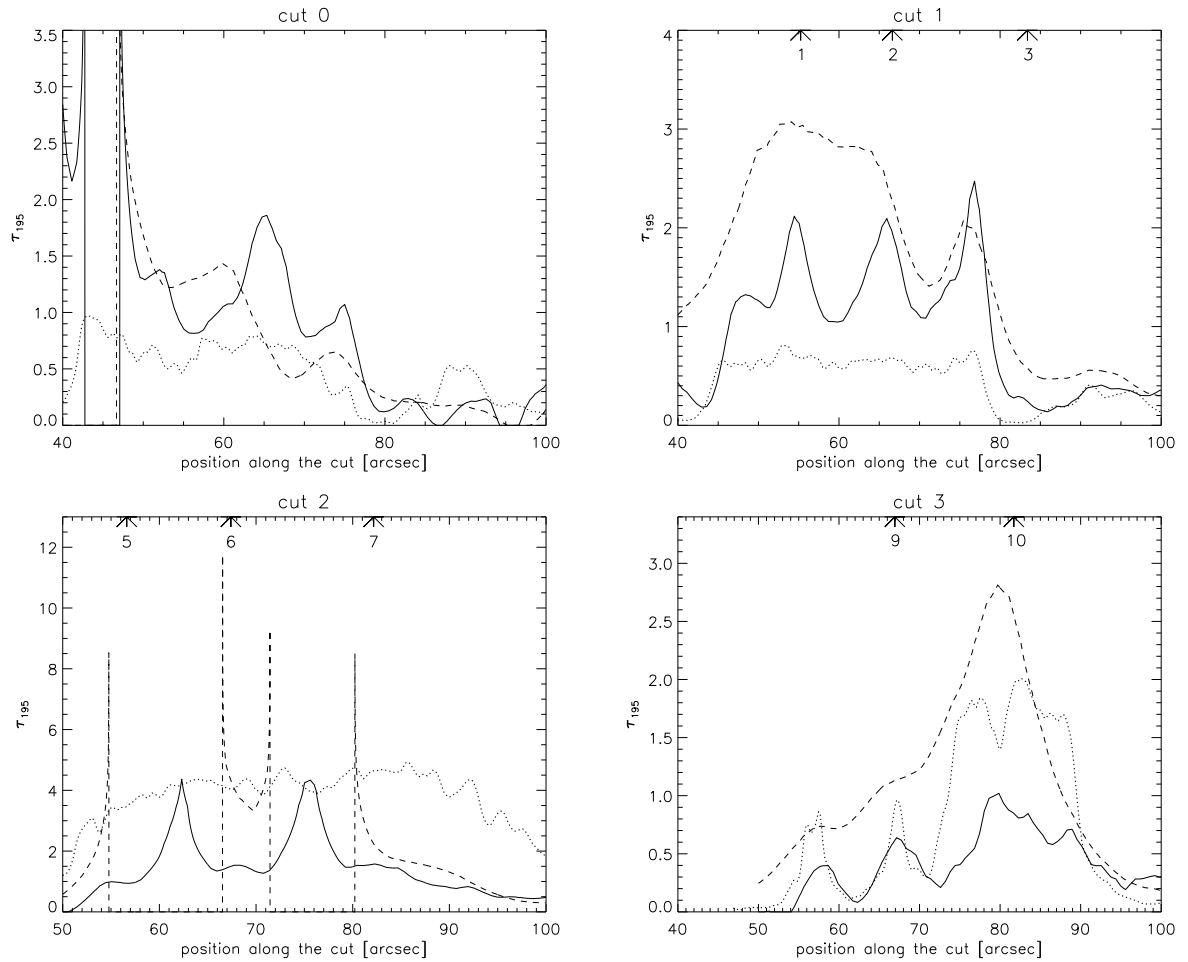
Fig. 8.— Plots of the optical thickness τ_{195} of the resonance continua at 195 Å along the individual cuts computed for $\alpha = 0.5$ from intensity ratios of TRACE 195 Å and XRT (full--lines) and from ratios of EIS (integrated over the TRACE bandpass) and XRT (dashed--lines). Dotted-lines show rescaled and vertically shifted distributions of the Hα emission as observed by SOT. Arrows at the top of the plots mark the positions of points shown in Fig. 4.
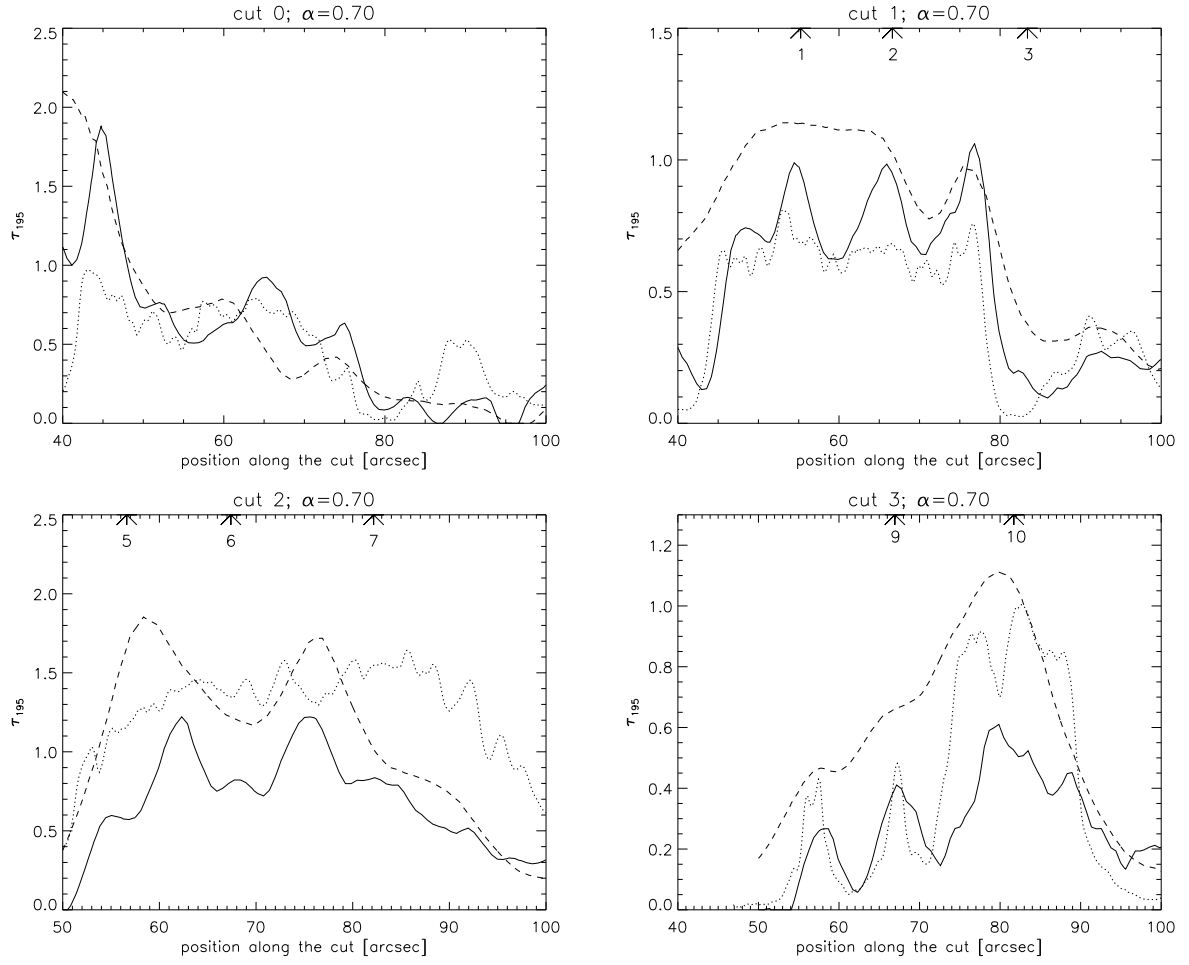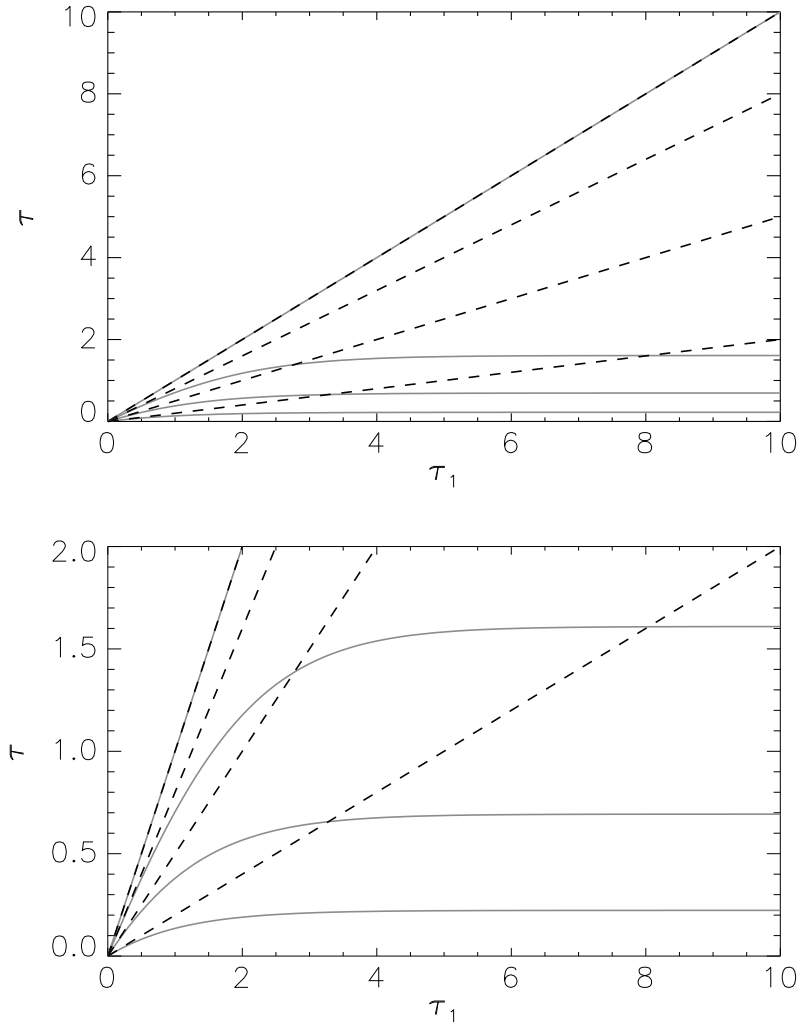
Fig. 9.— Same as in Fig. 8, but for $\alpha = 0.7$.

Fig. 10.— τ_1 is the actual optical thickness of the resonance continua at the wavelength position of EUV line under consideration, τ is the averaged thickness. Full lines correspond to the EUV case, dashed ones to Hα. Four curves correspond to four filling factors 1.0, 0.8, 0.5 and 0.2. The lower plot shows a zoom.